EXAFS and XANES spectroscopy study of the oxidation and deprotonation of biotite

BERND GÜTTLER,* WILHELM NIEMANN† AND SIMON A. T. REDFERN*

*Department of Earth Sciences, University of Cambridge, Downing Street, Cambridge CB2 3EQ, U.K.
†Haldor Topsøe Research Laboratories, DK-2800 Lyngby, Denmark

Abstract

The coupled thermal oxidation and deprotonation in air of iron-rich biotite (FeO + Fe_2O_3 = 34%) has been investigated by EXAFS and XANES spectroscopy at the Fe-*K* edge and by XANES spectroscopy at the Ti-*K* edge. Samples annealed for 5 h at temperatures between 250 °C to 600 °C have been studied. Distortions mainly of the Fe–Fe correlation within the octahedral layers are reflected in increasing Debye-Waller factors of the Fe–Fe correlation peak proportional to the annealing temperature. Unchanged Fe–O nearest-neighbour and Fe–Fe next-nearest-neighbour coordination numbers show that these distortions, nonetheless, do not change the structural topology of the octahedral layers. A model is introduced to demonstrate that increasing distortions are compatible with the expected heterogenous deprotonation mechanism in biotite. Titanium occurs in octahedral coordination. It was found to be unaffected by the coupled oxidation/deprotonation process. Both the coordination number and the valence state stay constant during the annealing process, in spite of dramatic changes of the Fe^{2+}/Fe^{3+} ratio. Thermally activated hopping conduction involving Ti according to $Fe^{2+}Ti^{4+} \rightarrow Fe^{3+}Ti^{3+}$ is, therefore, not a significant process during thermal deprotonation and oxidation in biotite.

KEYWORDS: EXAFS, XANES, deprotonation, layer silicates, biotite.

Introduction

BIOTITE is a sheet silicate which undergoes oxidation and deprotonation at elevated temperatures. In layer silicates such as kaolinite the deprotonation of the octahedral layers is known to be accompanied by the loss of structural oxygen, leaving former octahedral positions in a reduced coordination (e.g. Brindley and McKinstry, 1961; Iwai and Shimamune, 1975; Guggenheim *et al.*, 1987). The situation is different in ferrous biotite, however, because the electrostatic charge balance can be achieved by an iron-oxidation process. In contrast to the former case, no net oxygen transport within the crystal is necessary.

Though the deprotonation of biotite can be achieved locally by a coupled oxidation/deprotonation process within the octahedral layers, this process has been found to be greatly influenced by the atmospheric conditions during the thermal oxidation procedure. Annealing *in vacuo* increases the oxidation and deprotonation temperature by about 200 °C relative to an annealing process under ambient conditions (Sanz *et al.*, 1983). Atmospheric oxygen, therefore, is an important factor during oxidation and deprotonation of biotite.

The following formal reactions have been assigned to the different atmospheric conditions (Brindley and Lemaitre, 1987):

(i) Deprotonation and oxidation leading to the formation of hydrogen in the absence of an oxidizing atmosphere:

$$2Fe^{2+} + 2OH^- = 2Fe^{3+} + 2O^{2-} + H_2$$

(ii) Formation of water in the presence of oxygen:

$$4Fe^{2+} + 4OH^- + O_2 = 4Fe^{3+} + 4O^{2-} + 2H_2O$$

Water formation in biotite, therefore, is not generally an intrinsic process, but the question of how the water is formed can be discussed in the context of real dehydroxylation reactions in other layer silicates.

In general, two mechanisms have been established in order to explain the deprotonation kinetics of layer silicates (Brindley and Lemaitre, 1987):

(i) An homogeneous process involving the local

Mineralogical Magazine, December 1989, Vol. 53, pp. 591–602

formation of water throughout the whole volume of the crystal which can lead to a complete structural breakdown as observed in the metakaolinite phase.
(ii) A heterogeneous process in which the dissociation of OH-groups and the formation of water is locally delayed. This mechanism should leave the structure fairly unchanged (Pampuch, 1971).

The deprotonation process in biotite is generally looked upon as an ideal example of the latter process. The local deprotonation mechanism has been assumed to be independent of atmospheric conditions. The rate-determining step in the deprotonation process has been related to the transport kinetics of the protons (Sanz *et al.*, 1983).

The model of heterogeneous deprotonation in biotite has been further supported by single crystal and powder X-ray diffraction investigations. Ohta *et al.* (1982) investigated an oxybiotite by structure analysis and compared the result with a structural analysis of an artificially hydrogenated oxybiotite of the same origin (Takeda and Ross, 1975). They found the hydrogenated and dehydrogenated forms to be 'remarkably similar' and only the interlayer separation decreased. XRD powder measurements by Ferrow (1987) on synthetic annite $(KFe_3^{2+}(AlSi_3)O_{10}(OH)_2$ show slightly decreased *a* and *b* lattice constants during deprotonation which have been attributed to the substitution of the Fe^{2+} by the smaller Fe^{3+}. Reduced *c* values have been related to the loss of hydrogen in agreement with Ohta *et al.* (1982). No further effects of the deprotonation process were found.

From these and further spectroscopic studies, a model of the kinetic mechanism of the coupled oxidation-deprotonation has evolved. Addison and Sharp (1962) had already suggested separate electron and proton hopping processes to the crystal surface. Vedder and Wilkins (1969) preferred a coupled hopping process of electrons and protons due to mobility considerations. The possibility of Fe^{2+}–Fe^{3+} hopping processes (*intervalence–charge–transfer*, IVCT) in biotite has been further supported by optical spectroscopy (Robbins and Strens, 1968; Faye, 1968*a*; Smith *et al.*, 1980) and conductivity measurements (Davidson and Yoffe, 1968; Meunier *et al.*, 1983).

The extent to which the structure is affected by the deprotonation is still unclear, however. Mössbauer studies show increased quadrupole splittings and line-widths, which indicate distortions of the iron octahedra after deprotonation (Heller-Kallai and Rozenson, 1980; Bagin *et al.*, 1980). Also, the model of a purely heterogeneous deprotonation mechanism has been undermined by the observation of a true dehydroxylation due to the loss of OH groups and the subsequent formation of water even below 500 °C (Sanz *et al.*, 1983; Vedder and Wilkins, 1969; Rouxhet *et al.*, 1972). Furthermore, discrepancies between TEM (Wirth, 1985) investigations and structure analysis (Guggenheim *et al.*, 1987) of muscovite left some doubts about the capabilities of either of the two methods. Structure analysis is relatively insensitive to non-periodic distortions which might result from water transport during deprotonation. Such distortions have been observed by Wirth (1985) using transmission electron microscopy and have been related to the deprotonation, but Guggenheim *et al.* (1987) suggested that these observations might arise from electron beam damage. The role of minor constituents which may affect the deprotonation significantly, either by their different valence state or by controlling the number of vacancies in the structure (Hazen and Burnham, 1973), must also be considered. Detailed information about deprotonation and its structural effect is needed, therefore, before we can claim a real understanding of such processes in complex systems like natural layer silicates.

EXAFS and XANES spectroscopy provide information about selected elements concerning their valence state and the distances and coordination numbers of at least two coordination spheres. In particular, the potential of EXAFS spectroscopy in determining ordering conditions on a short and intermediate scale in iron oxides and oxyhydroxides has recently been emphasised (Manceau and Combes, 1988). These methods are, therefore, able to match simultaneously a number of needs crucial for the study of deprotonation in layer silicates, without any loss of specificity. The usefulness of these methods in this context, especially in connection with other spectroscopical tools, such as infrared spectroscopy, will be demonstrated as we attempt to shed further light on the deprotonation and oxidation processes in biotite.

Experimental procedure

Experimental setup. The experiments were performed at the EXAFS II beamline of the HASYLAB (Hamburger Synchrotronstrahlungslabor) which is part of the DESY (Deutsches Elektron-Synchrotron) in Hamburg, West Germany. The DORIS II (Doppel-Ring Speicheranlage) storage ring is used as the light source for the HASYLAB.

A 1:1 image of the source spot in the ring is produced via four toroidal gold mirrors (glancing angle = 7 mrad) and focused onto a double crystal (Si 111) mono-

chromator allowing an energy range of 2 keV to 12 keV and a spectral resolution of 1.5 eV at 7 keV. Three consecutive ionization chambers are used in order to perform simultaneous measurements of a sample spectrum and a reference spectrum. This allows for a relative accuracy of the energy scale of 0.1 eV. The photon flux at the sample position is 10^{11} photons/(sec eV) in the 5–7 keV range. The monochromator setting as well as the data collection is interactively controlled by a PDP 11/23 computer via a CAMAC interface.

Further details of the EXAFS II beamline have been described elsewhere (Niemann *et al.*, 1987, and references therein).

Data collection. EXAFS spectra were obtained from 250 eV below to 1000 eV above the Fe–*K* edge. An automatically set spectral step-width was used. It was varied between 1 eV in the vicinity of the edge (−35 eV to +75 eV) up to 5 eV further from the edge (>600 eV) by increasingly broader stepwidths.

XANES spectra of the Fe–*K* edge and the Ti–*K* edge were recorded from the same samples as used for the EXAFS measurements. Data within a range of 110 eV in the vicinity of the *K* edge were recorded using a step-width of 0.2 eV.

Sample preparation. A natural, pegmatitic single crystal of iron-rich biotite (*ca.* $1 \times 1 \times 2.5\,cm^3$) of unknown origin was selected from the mineral collection of the Universität Hannover (West Germany) as starting material. Electron diffraction techniques revealed a 2 *M* polytype.

The starting material was cut into flakes parallel to the cleavage planes and mechanically ground (15 min) in an agate cylinder using an electric mill (Spex) to obtain a final grain size of 2 to 4 μm. The grain size and its homogeneity were each carefully checked by optical microscopy. 200 mg biotite powder was produced and used for further annealing.

The powder was then annealed in air at different temperatures by using a constant heat ramp of 100 °C per hour up to the final temperature of each specific run. Each sample remained at its final temperature for 5 h and was subsequently quenched in air.

The annealed powder samples were then mixed with polyethylene powder (BDH) (sample/reference: 1/10). This was carried out in a similar manner to the grinding procedure described above, but no grinding balls were used. The resulting mixture was then pressed into pellets (10 tons/cm², 13 mm diameter) using a die (Perkin Elmer). This procedure is very similar to the preparation of powder samples for far-infrared spectroscopy. It allows ideally homogeneous sample distributions within the pellets to be obtained and avoids preferential orientations due to the platelet-like cleavage of biotite. Sample powder embedded in wax gave similar EXAFS and XANES spectra but of poorer quality due to poorer homogeneity.

Methods of sample characterization. The changing Fe^{2+}/Fe^{3+} ratios were followed by standard photometrical analytical methods after decomposition in hydrofluoric acid. The deprotonation was investigated by IR spectroscopy of KBr pellets in the OH-stretching mode region. The spectra were recorded on a Bruker 113v Fourier-transform spectrometer.

TABLE 1. Chemical analysis of the starting material

Element	Element weight %	Oxide weight %
Na	0.29	0.39
Mg	1.42	2.36
Al	5.81	10.99
Si	16.39	35.06
K	7.20	8.68
Ti	2.26	3.77
Mn	1.23	1.58
Fe^{2+}	21.02	27.04
Fe^{3+}	4.93	7.05
	60.55	96.92
+ H_2O^+		3.4
		100.32

Results

Characterization of the starting material. The starting material was chemically analysed to an overall accuracy better than 1% by electron microprobe analysis using an energy dispersive detector which allowed for the analysis of elements heavier than fluorine. The chemical formula, based on 24 (O,OH), may be written as:

$$Na^{+}_{0.12}K^{+}_{1.81}[Fe^{2+}_{3.52}Fe^{3+}_{0.83}Ti^{4+}_{0.46}Mg^{2+}_{0.57}Mn^{2+}_{0.22}\square_{0.4}]$$
$$(Al^{3+}_{2.12}Si^{4+}_{5.73}O^{2-}_{20})O^{2-}_{0.26}(OH)^{-}_{3.74}.$$

Several analyses have been carried out at maximum distances of 1 cm parallel as well as perpendicular to the crystal column by investigating flakes cut out of the single crystal. No significant spatial differences of the chemical composition could be found. Atomic absorption spectroscopy and electrochemical investigations did not reveal significant amounts of lithium or fluorine. Fe^{2+}/Fe^{3+} ratios were determined photometrically for the starting material as well as for all subsequently annealed samples. A full analysis is given in Table 1.

Characterization of the annealing process. The photometrically determined Fe^{2+}/Fe_{total} ratios of the various states of the annealing process are given in Fig. 1. The protron-loss process was followed by IR spectroscopy of the OH-stretching band. The intensity of these bands, determined

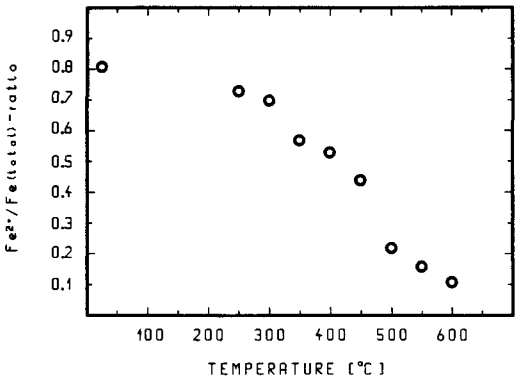

FIG. 1. Photometrically determined Fe^{2+}/Fe_{total} ratios of powdered biotite after 5 h annealing time at a given temperature.

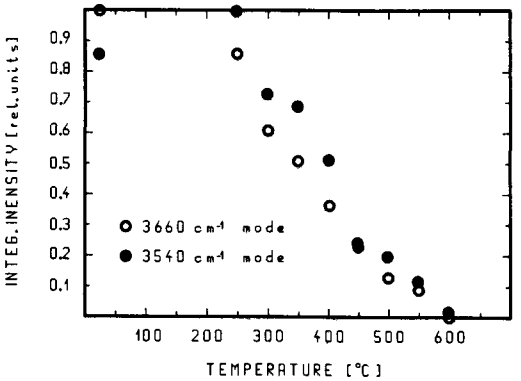

FIG. 2. Integrated intensities of the OH-stretching modes of powdered biotite after 5 h annealing time at a given temperature as determined from line profile analysis.

by line profile analysis, is shown in Fig. 2. The spectra are shown in Fig. 3.

The starting material has an Fe^{2+}/Fe_{total} ratio of 0.81. The infra-red spectra show the main trioctahedral vibration of 3661 cm^{-1} and the dioctahedral vibration at 3540 cm^{-1}. These frequencies correspond almost exactly to those of synthetic annite ($KFe_3^{2+}AlSi_3O_{10}(OH)_2$) as found by Farmer (1971). The high intensity of the dioctahedral vibration peak relative to that of the trioctahedral peak reflects the much higher absorption cross-section of the former peak, in agreement with previous investigations (e.g. Sanz *et al.*, 1983).

Both deprotonation and oxidation start at temperatures as low as 250 °C. The oxidation state was found to change most significantly between 300 and 500 °C and is almost completed at 600 °C. The Fe^{2+}/Fe_{total} ratio after annealing at this temperature is 0.11 and the hydroxyl bands in the IR spectra have vanished. This confirms the coupling between oxidation and deprotonation suggested by earlier experiments.

The temperature dependence of our experimental data is in agreement with results of Bagin *et al.* (1980), obtained on biotite powders annealed for similar periods of time. The higher deprotonation temperatures found by Sanz *et al.* (1983) can be related to their shorter annealing times.

The deprotonation behaviour found by the latter authors is nonetheless in qualitative agreements with our results. It is characterized by the loss of protons from trioctahedral sites prior to the loss of protons from dioctahedral sites, the latter process not being significant below 400 °C. The intensity of the peak related to trioctahedral sites continuously decreased, starting at temperatures of 250 °C. No frequency shifts of this peak during deprotonation were found. Sanz *et al.* (1983) concluded from a similar observation that some real dehydroxylation occurs in biotite, because otherwise an increase of the ($R^{2+}R^{2+}R^{3+}$–OH) vibration at the expense of the ($R^{2+}R^{2+}R^{2+}$–OH) vibration should occur.

EXAFS (Fe–K edge). Data from 50 eV above the Fe–*K* edge have been used for the Fourier transformation of the EXAFS interference function $\chi(k)$, the normalized part of the X-ray absorption coefficient. The coordination number N_j the distance R_j and the mean-square displacement σ_j^2 of the first two shells surrounding the iron sites have been calculated separately from Fourier backtransformations of the resulting radial distribution function by using Bessel windows and standard Fourier-transform and linear least-square fit procedures. This process has been described in more detail by Niemann *et al.* (1987). The backscattering amplitude $F_j(k)$ and the phase shift $\Phi_j(k)$ of the j-th neighbour shell have been calculated from the starting material by using coordination numbers and distances obtained from structural analysis (Hazen and Burnham, 1973). Negligible displacements of the shells have been assumed. Care was taken that each spectrum was computed with identical parameters. A VAX 750 computer was employed for the calculations.

The absorption spectra of the starting material and the completely deprotonated sample are shown in Fig. 4. The corresponding radial distribution functions (RDFs) of the whole sequence are shown in Fig. 5. The spectrum of the starting material closely resembles those of annite and biotite as measured by Bonnin *et al.* (1985), indicating their overall comparability with similar

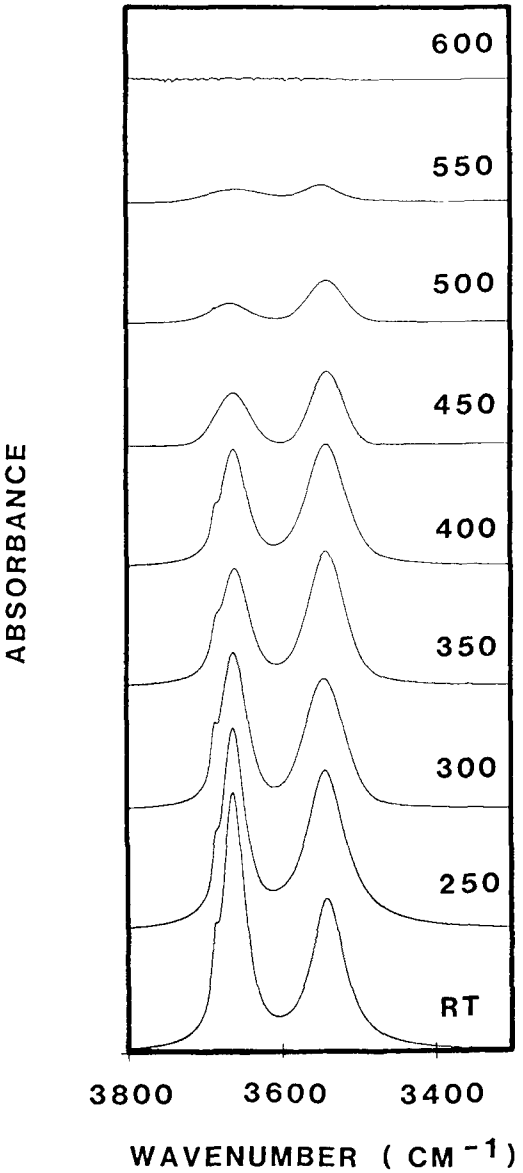

FIG. 3. Temperature evolution of the OH-stretching modes of powdered biotite after 5 h annealing time at a given temperature.

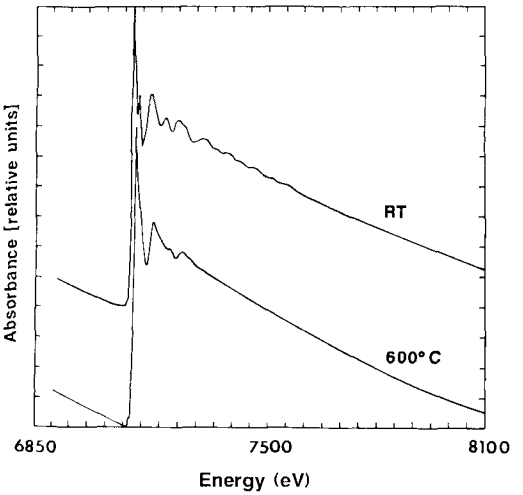

FIG. 4. Fe–*K* edge EXAFS spectra of the starting material (RT) and of completely deprotonated sample (600 °C).

degrees of order in the untreated material. The RDF of the starting material is characterized by two peaks which can be correlated to the nearest-neighbour (oxygen) and next-nearest-neighbour (iron) shells relative to iron. A third peak can also be found which has been related to the next-nearest iron distances (second-nearest iron shell) by the latter authors. The higher intensity of the second correlation peak (iron–iron) relative to the first correlation peak (iron–oxygen) in spite of similar coordination numbers indicates the higher backscattering amplitude of iron relative to oxygen. The deprotonation/oxidation process is mainly characterized by a decrease of the second correlation peak (iron–iron) of almost 60%.

The results from the fitted Fourier backtransformation of the iron–oxygen correlation peak are shown in Fig. 6. Constant coordination numbers within the experimental accuracy (10%) were found during the deprotonation/oxidation whereas the Fe–O distances decrease from 2.11 Å as assumed in the starting material from structure analysis (Hazen and Burnham, 1973) to 2.02 Å in the oxidized material. The decrease follows the changing Fe^{2+}/Fe^{3+} ratios reasonably well and the final distance is in agreement with Fe^{3+}–O distances as generally found in octahedral environments (e.g. Beran and Bittner, 1974) and is significantly larger than Fe^{3+}–O distances found in tetrahedral environments (e.g. cronstedtite, 1.85 Å: Geiger *et al.*, 1983; Calas *et al.*, 1984). The Fe–O EXAFS indicate, therefore, that the Fe–O octahedra remain intact although increasing distortions can be detected by increasing Debye-Waller factors.

The decreasing Fe–Fe correlation peak is characterized by a very large increase of the mean square displacements whereas the mean distances as well as the coordination numbers remain constant within the experimental accuracy (0.02 Å, 15%, respectively) (Fig. 7). The decreasing iron–

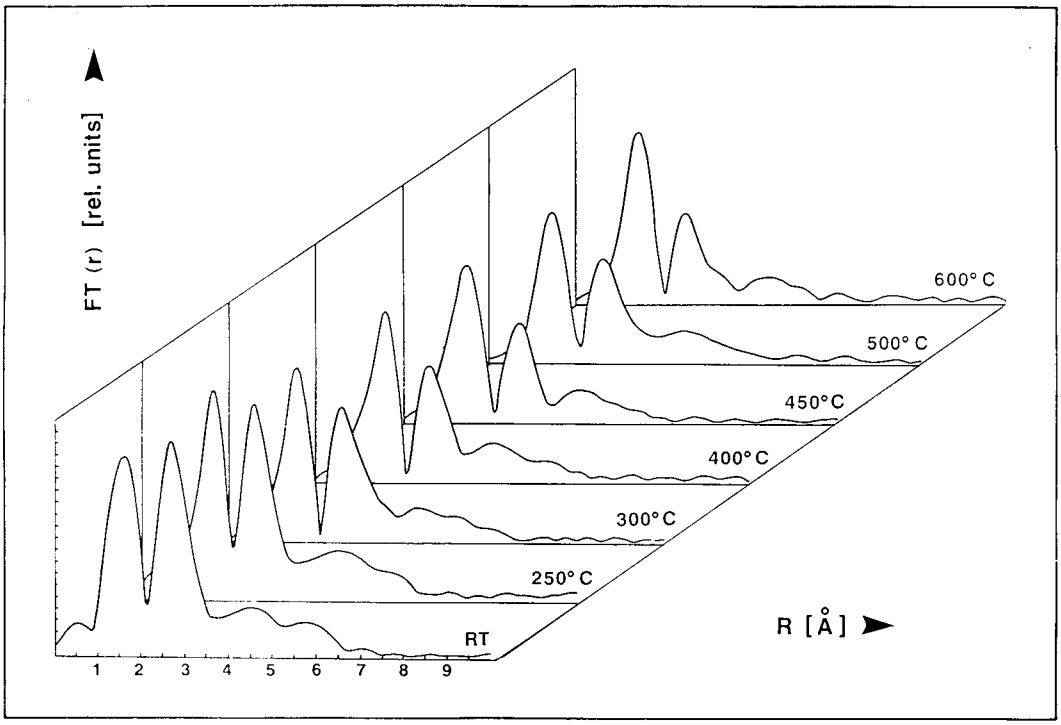

FIG. 5. Fourier transforms (radial distribution functions) of the Fe–*K* edge EXAFS spectra of powdered biotite after 5 h annealing time at a given temperature.

iron correlation peak found in the RDFs, therefore, can be related to structural distortions of the iron–octahedra network. This result is consistent with the XANES spectra (see below) and Fe–O EXAFS spectra which do not indicate significant amounts of iron in an amorphous iron oxide phase which would result from a release of iron from the octahedral sheets.

A further interpretation of the annealing process, therefore, has to be based on the maintenance of the structural topology within the layers. Hence, the distortions are mainly caused by effects which distort the layers as a whole rather than a destruction within the layers. We do not observe the structural breakdown which occurs during the dehydroxylation of kaolinite into the metakaolinite phase (Brindley and McKinstry, 1961) which would point to a homogeneous dehydroxylation process. But the results from the Fe–Fe correlation peak of the EXAFS spectra clearly indicate that the generally assumed model of a purely heterogeneous deprotonation process, with a simple proton–electron transport process to the crystal surface without affecting the crystal structure is insufficient to explain the annealing process. Our results suggest an irregular undulation of the structural sheets caused by a partial interlamellar swelling. As the only significant chemical changes during the annealing process are the losses of constitutional protons and a small amount of hydroxyl groups (i.e. including structural oxygen), it seems reasonable to relate the swelling to the genesis of water. A coupled oxidation–deprotonation process alone cannot result in the formation of water. The formation of small amounts of water during the annealing process of biotite, however, is well known (Rouxhet *et al.*, 1972; Sanz *et al.*, 1983). In addition, micas are known to be highly hygroscopic and usually contain a fair amount of water if they are not artificially dried out (see e.g. Meunier *et al.*, 1983). This water is likely to be introduced parallel to the sheets into the interlamellar voids of the micas. Small regions of the structure, therefore, should already be distorted in the previously described manner even in the natural, unheated starting material.

The unbound water within the distorted regions of the crystal escapes parallel to the sheets during the annealing process at low temperatures

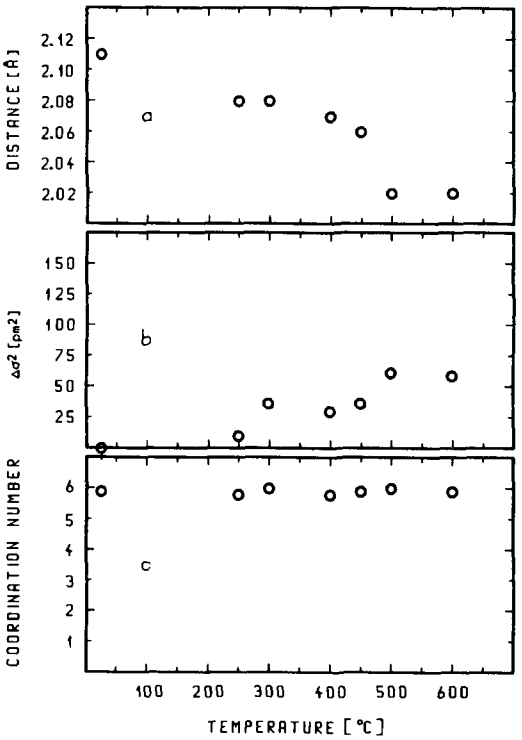

FIG. 6. The distances (*a*), mean-square displacements (*b*) and coordination numbers (*c*) of the nearest neighbour shell (oxygen) as determined from the fitted Fourier backtransforms of the Fe-*K* edge EXAFS of powdered biotite after 5 h annealing time at a given temperature.

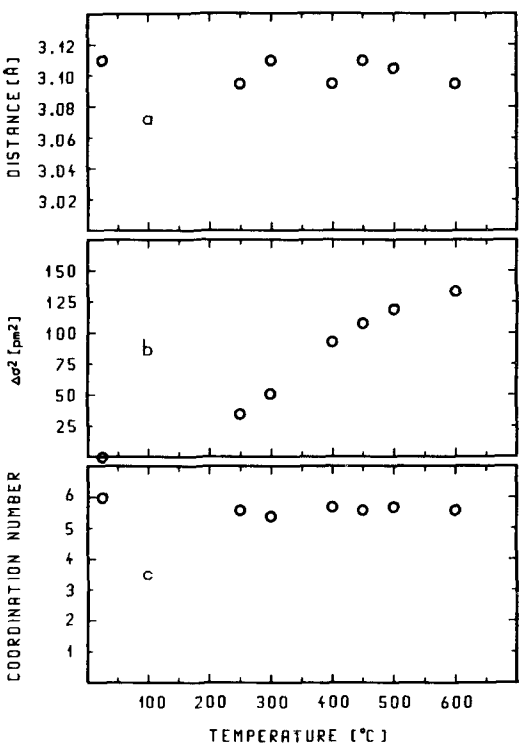

FIG. 7. Same as Fig. 6 for the next-nearest neighbour shell (iron).

(~200 °C), resulting in a further increase of the distortions in the vicinity of the already distorted regions.

Further annealing at increasing temperatures leads to a release of protons as OH bonds are broken and a proton transport is introduced most likely via a hopping process as suggested by Addison and Sharp (1962). This hopping transport, however, is largely hindered in the absence of energetically equivalent sites in their vicinity and is, therefore, hindered within the distorted regions of the crystal. Trapping of the protons in those regions can therefore be assumed. Also, the formation of water caused by the loss of OH groups, although a minor process in biotite, should occur more readily where the proton motion is difficult. Simultaneously with the loss of unbound water parallel to the sheets, oxygen from the surrounding atmosphere can penetrate inwards into the crystal through the same distorted interlamellar regions resulting in further water formation by a reaction with the trapped protons.

Distortions, therefore, would have to be looked upon as additional surfaces and should grow during the deprotonation process. In the course of deprotonation the initial distortions act as nucleation centres for further distortions which initially grow parallel to the sheets and then, although much more slowly, perpendicular to the sheets.

This model is in agreement with electron-microscopic observations on phengite (Wirth, 1985) and TEM and HRTEM investigations on our own material (Putnis and Güttler, in preparation). We conclude, therefore, that the observed structural distortion can only sensibly be linked to the formation of water.

XANES spectroscopy. Although the theoretical background of XANES spectroscopy is still somewhat unclear, detailed information about coordination numbers and distortions of the first coordination shell and the valence state of the central atom can be obtained from a comparison with well-known model substances. Conve-

niently, two main features in the spectrum are distinguished:

(i) a pre-edge region may exhibit peaks at energies 10–20 eV below the edge-crest. Their intensity is to a first approximation inversely proportional to the centre-symmetry of the first coordination shell. They are therefore believed to obey the Laporte selection rule and are generally assigned to 1*s*–3*d* transitions.

(ii) the main edge region has been related either to transitions to empty, bonded states of *MO* character (e.g. Tossel *et al.*, 1974) or to multiscattering effects (Durham *et al.*, 1982; Norman *et al.*, 1985).

Fe–K edge. XANES spectra of the Fe–*K* edge are shown in Fig. 8. The pre-peak intensity which is similar to pre-peak intensities of Fe^{2+} in regular sites as in wüstite (Calas *et al.*, 1984).

As 19% of the total iron content in the starting material is Fe^{3+}, we must address the possibility that some may be in tetrahedral coordination. Tetrahedral Fe^{3+} is known to produce a tenfold increase of the pre-peak intensity relative to that in octahedral sites (Waychunas and Rossman, 1983). This increase corresponds to our own measured values using magnetite as a standard (3.7-fold intensity with one-third of total iron in tetrahedral coordination). In view of the error in the pre-peak intensity measurements of ±10%, the amount of tetrahedral iron in the starting material cannot exceed 3% of the total iron. This result confirms that Fe^{3+} is strictly not occupying tetrahedral sites as long as the amount of Al and Si is sufficient to fill up these sites.

The pre-peak intensities increase only slightly during the coupled oxidation/deprotonation process (~30 ± 10% increase). Such changes may correspond to generally increased distortions of the octahedral sites as already suggested by structure analysis and Mössbauer spectroscopy (Ohta *et al.*, 1982; Heller-Kallai and Rozenson, 1980; Bagin *et al.*, 1980). No evidence for decreasing coordination numbers could be found. At least 90% of the iron remains in a sixfold coordination. The result is confirmed by the spectral measurements in the edge crest region. The XANES spectrum of the starting material closely resembles that of Fe^{2+} octahedra in annite in this frequency range. With increasing annealing times a crossover can be observed resulting in a shape close to that of Fe^{3+} octahedra in nontronite (Bonnin *et al.*, 1985). No further effects have been detected.

Hence, XANES spectroscopy confirms the results of the EXAFS spectroscopy described above. Coordination numbers remain constant

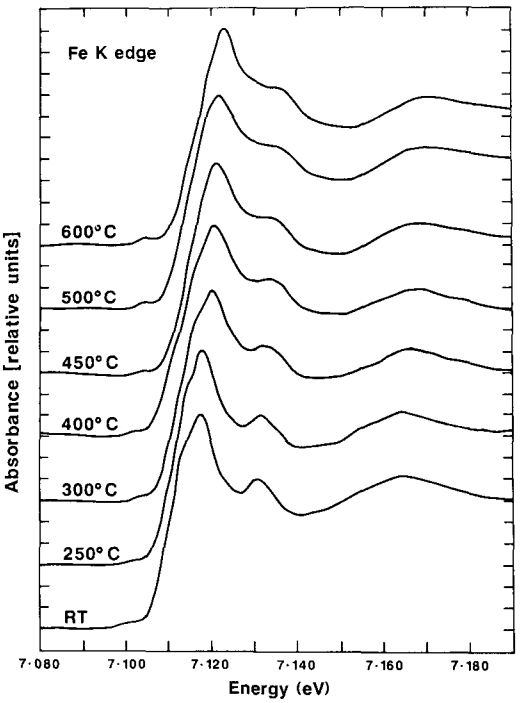

FIG. 8. Fe–*K* edge XANES spectra of powdered biotite after 5 h annealing time at a given temperature.

within the experimental error; real dehydroxylation due to local water formation must be small (<10%) and no evidence has been found for the evolution of amorphous iron oxide which is known to enclose Fe^{3+} in a fourfold coordination (Calas and Petiau, 1983).

Ti–K edge. The importance of titanium, although a minor constituent in biotite, stems from its potential role in controlling the number of vacant cationic sites by a coupled substitution process (Thompson, 1973):

$$Ti^{4+} + \square = 2\,(Fe^{2+},Mg^{2+})$$

Such vacancies may have a significant influence on the deprotonation and oxidation process of biotite. The investigation of such a process, however, relies on the assumptions that titanium occurs only in octahedral coordination and the proportion of titanium in an oxidation state lower than Ti^{4+} is insignificant. Charge transfer processes between iron and titanium of the form

$$Fe^{2+} + Ti^{4+} \rightarrow Fe^{3+} + Ti^{3+}$$

have, however, been proposed, based on optical spectroscopy (Faye, 1968*a*,*b*; Rossman, 1984) and *MO* calculations (Sherman, 1987).

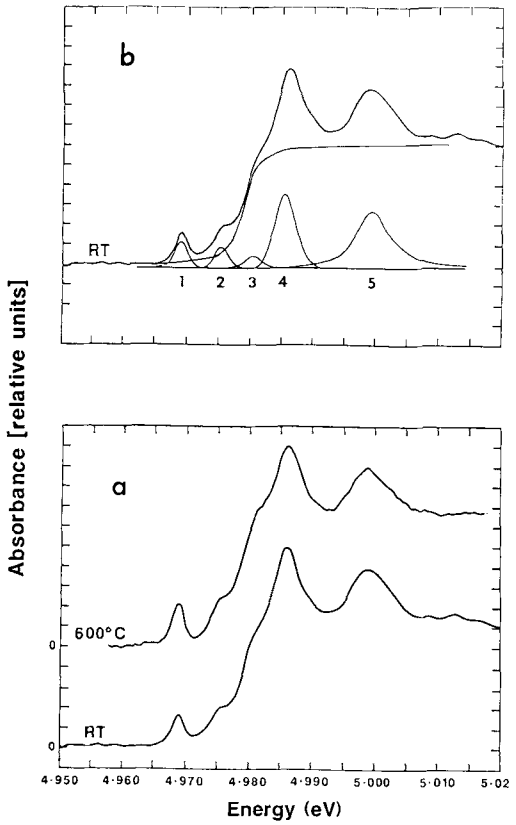

FIG. 9. Ti–*K* edge XANES spectra of powdered biotite: (*a*) before and after 5 h annealing at 600 °C; (*b*) line profile analysis before annealing.

TABLE 2. Results of the least-square fit procedure on the Ti *K* -edge (peak assignment according to Fig. 9 b)

	Peak Positions (eV)	
Peak	Starting material	Annealed at 600 °C
1	4968.9	4968.8
2	4975.4	4975.5
3	4981.2	4981.3
4	4986.3	4986.3
5	4999.2	4998.6
	Intensities (rel. units)	
1	0.129	0.187
2	0.103	0.124
3	0.065	0.099
4	0.369	0.357
5	0.282	0.257
step function	0.647	0.676

Titanium is also known to exist in different coordination environments for varying concentration levels in TiO_2–SiO_2 glass, with a predominantly tetrahedral coordination in a concentration range between 0.05 and 9% TiO_2 in the glass mixture (Greegor *et al.*, 1983). This value corresponds to a TiO_2 content of 3.8% in the biotite studied here. The role of titanium during the annealing process cannot, therefore, be ignored.

XANES spectra of the Ti–*K* edge of the starting material and of the completely deprotonated/oxidized material were recorded and fitted by using Voigt profiles (Fig. 9). The results are listed in Table 2. Although essentially similar to the Fe–*K* edge, the Ti–*K* edge is more pronounced and allows a more detailed analysis. This is because the probability of transition to the final 3*d* states is higher due to the low number of occupied 3*d* states (Waychunas *et al.*, 1983). The pre-edge peak intensities are greater than for Fe by one order of magnitude in the starting material (1.2% of edge crest intensity at the Fe–*K* edge *vs.* 12.9% at the Ti–*K* edge). After oxidation and deprotonation the pre-peak intensity has increased by about one-third to 18.7% of the edge crest intensity.

Two shoulders can be identified at the edge threshold on the low-energy side of the edge crest. They can be fitted as Gaussian profiles and, as for the pre-peak, we see that their intensities increase by roughly one-third during deprotonation/oxidation. Energetically, the first peak corresponds reasonably well to transitions to the $7a_{1g}$– or $7t_{1u}$–*M*O-orbitals as calculated by Tossel *et al.* (1974) which may have some 4*s* character and, therefore, also obey the Laporte selection rule. Other interpretations, however, assign these features as coupled excitations (Waychunas, 1987) or multiple scattering effects as described previously (Durham *et al.*, 1982; Norman *et al.*, 1985).

Waychunas (1987) demonstrated, that Ti pre-peak intensities can be reasonably well correlated to octahedral site distortions. Ti pre-peak intensities of octahedral sites are, for example, as large as 25% of the edge crest intensity in the strongly distorted sites of kaersutite and neptunite. According to their empirical diagram the pre-peak intensity of an untreated biotite with a static

bond angle variance of 26.4 deg^2 as determined from structure analysis (Hazen and Burnham, 1973) should give a pre-peak intensity of 13 ± 5% of the edge crest intensity, whereas a deprotonated/oxidized biotite, with a bond angle variance of 31.7 deg^2 (Ohta *et al.*, 1982) should give a pre-peak intensity of 17 ± 5%. These figures are in excellent agreement with our own measured values (12.9 ± 1% for the untreated biotite *vs.* 18.9 ± 1% for the completely deprotonated biotite). Ti in a purely tetrahedral coordination would give a pre-peak intensity of 70% (Ba_2TiO_4, Greegor *et al.*, 1983). Our results therefore demonstrate that Ti occurs in an octahedral coordination before and after the annealing process (just like Fe). The proportion of tetrahedrally coordinated Ti is insignificant (less than 5%). The sixfold coordination remains intact in at least 90% of the Ti octahedra.

The valence state of Ti in biotite can be deduced from the pre-peak energy shift. Waychunas (1987) found this peak shifted about 2 eV towards higher energies on changing from Ti^{3+} to Ti^{4+}. Similar values have been determined from EELS at the Ti–L_3 edge (Otten and Buseck, 1987). The possible influence of *intervalence charge transfer* (IVCT) process between iron and titanium can be verified by this shift.

The Fe^{2+}/Fe_{total} ratio in our oxidized biotite is 0.11, which practically excludes the existence of Ti^{3+} states in this material. The untreated biotite, on the other hand, exhibits an Fe^{2+}/Fe_{total} ratio of 0.81 with small amounts of Ti within the Fe network. Any shift of the pre-peak of the oxidized biotite relative to the untreated biotite, therefore, should indicate Ti^{3+} states in the untreated biotite. No such shifts could be found, however, within the experimental accuracy (±0.1 eV). The valence state of titanium is not affected by the annealing process. The amount of Ti^{3+} in the starting material certainly cannot be greater than 10% of the total Ti content.

This result is in agreement with the observations of Waychunas (1987) and Otten and Buseck (1987) which do not indicate any evidence for Ti^{3+} in natural, terrestrial iron minerals (in contrast to meteoritic and lunar minerals). The suggested band assignment of the optical spectra as Fe → Ti IVCT bands may be correct, but our results indicate a vanishing occupation density of such optically excited states.

It can be concluded, therefore, that titanium is not involved in the deprotonation process although it is indeed enclosed in octahedral lattice sites. Both valence state and coordination number stay constant during annealing.

This leads to the assumption that the Ti–O octahedra are already mainly deprotonated in the starting material. Thompson's substitution model may, nonetheless, be justified, as Ti and vacancy sites may interact via electron–proton transport processes during crystal growth close to thermodynamic equilibrium. Hazen and Burnham (1973) pushed this substitution model even further, however, and suggested a short-range ordering process leading to the formation of titanium–vacancy pairs in order to achieve a local electrostatic charge balance. This is in disagreement with our results.

Conclusions

The generally assumed coupled deprotonation/oxidation mechanism of ferrous biotite is confirmed by EXAFS and XANES spectroscopy. The deprotonation process should, however, lead to severe structural distortions. They occur on an intermediate scale and leave the coordination polyhedra fairly unaffected. Such distortions do not result from a simple heterogeneous deprotonation mechanism but can be understood as a consequence of native structural imperfection.

EXAFS and XANES spectroscopy has also provided specific information about minor structural constituents like titanium. Their behaviour may differ entirely from that of the major constituents occupying the same crystallographic sites. In the case of titanium it differs to the extent that the Ti polyhedra simply do not take part in the deprotonation process whose principal local mechanism, the coupled oxidation/deprotonation process, is entirely controlled by the major constituent iron.

Acknowledgements

BG is thankful for support by NERC, EEC and the DFG via SFB173. SATR acknowledges funding from the Harkness Scholarship. We are indebted to the HASYLAB (Hamburger Synchrotronstrahlungslabor) for providing beam time at the EXAFS II-experiment. Many thanks to Dr Ronald Frahm for his support and helpful discussions during the experiments.

References

Addison, C. C. and Sharp, J. H. (1962) Mechanism for the oxidation of ferrous iron in hydroxylated silicates. *Clay Mineral. Bull.* **5**, 73–9.

Bagin, V. I., Gendler, T. S., Dainyak, L. G. and Kuz'min, R. N. (1980) Mössbauer, thermomagnetic and X-ray study of cation ordering and high-temperature decomposition in biotite. *Clays and Clay Minerals* **28**, 188–96.

Beran, A. and Bittner, H. (1974) Untersuchungen zur Kristallchemie des Ilvaits. *Tscherm. Min. Petr. Mitt.* **21**, 11–29.

Bonnin, D., Calas, G., Suquet, H., and Pezerat, H. (1985) Site occupancy of Fe^{+} in garfield nontronite: a spectroscopic study. *Phys. Chem. Minerals* **12**, 55–64.

Brindley, G. W. and Lemaitre, J. (1987) Thermal oxidation and reduction reactions of clay minerals. p. 319–70. In *Chemistry of Clays and Clay Minerals* (A. C. D. Newman, ed.), *Mineralogical Society Monograph* No. 6, 319–70.

——and McKinstry, H. A. (1961) The kaolinite mullite reaction series: IV The coordination of aluminium. *J. Am. Ceram. Soc.* **44**, 506–7.

Calas, G. and Petiau, J. (1983) Coordination of iron in oxide glasses through high-resolution *K*-edge spectra: Information from the pre-edge. *Solid State Commun.* **48**, 625–9.

——Basset, W. A., Petiau, J., Steinberg, M., Tchoubar, D. and Zarka, A. (1984) Some mineralogical applications of synchrotron radiation. *Phys. Chem. Minerals* **11**, 7–36.

Davidson, A. T. and Yoffe, D. (1968) Hopping electrical conduction and thermal breakdown in natural and synthetic mica. *Phys. Stat. Sol.* **30**, 741–54.

Durham, P. J., Pendry, J. B. and Hodges, C. H. (1982) Calculation of X-ray absorption near-edge structure. XANES. *Comput. Phys. Commun.* **25**, 193–205.

Farmer, V. C. (1971) The layer silicates. In *Infrared spectra of minerals* (V. C. Farmer, ed.), *Mineralogical Society Monograph* No. 4.

Faye, G. H. (1968*a*) The optical absorption spectra of iron in six-coordinate sites in chlorite, biotite, phlogopite and vivianite. Some aspects of pleochroism in sheet silicates. *Can. Mineral.* **9**, 403–25.

——(1968*b*) The optical absorption spectra of certain transition metal ions in muscovite, lepidolite and fuchsite. *Can. J. Earth Science* **5**, 31–8.

Ferrow, E. (1987) Mössbauer and X-ray studies on the oxidation of annite and ferriannite. *Phys. Chem. Minerals* **14**, 270–5.

Geiger, C. A., Henry, D. L., Bailey, S. W. and Maj, J. J. (1983) Crystal structure of cronstedtite-$2H_2$. *Clays and Clay Minerals* **31**, 97–108.

Greegor, R. B., Lytle, F. W., Sandstrom, D. R., Wong, J. and Schultz, P. (1983) Investigation of TiO_2–SiO_2 glasses by x-ray absorption spectroscopy. *J. Non-Cryst. Solids* **55**, 27–43.

Guggenheim, S., Chang, Y. and Koster van Groos, A. F. (1987) Muscovite dehydroxylation: High-temperature studies. *Am. Mineral.* **72**, 537–50.

Hazen, R. M. and Burnham, C. W. (1973) The structure of one-layer phlogopite and annite. Ibid. **58**, 889–900.

Heller-Kallai, L. and Rozenson, I. (1980) Dehydroxylation of dioctahedral phyllosilicates. *Clays and Clay Minerals* **28**, 355–68.

Iwai, S. and Shimamune, T. (1975) X-ray studies of the metakaolin state of dickite. In *Contributions to clay mineralogy dedicated to Professor Toshio Sudo* (K. Henmi, ed.), 30–3. Tokyo University of Education, Bunkio-Ku, Tokyo.

Manceau, A. and Combes, J. M. (1988) Structure of Mn and Fe oxides and oxyhydroxides: A topological approach by EXAFS. *Phys. Chem. Minerals* **15**, 283–95.

Meunier, J. F., Currie, M. R., Wertheimer, M. R. and Yelon, A. (1983) Electrical conduction in biotite micas. *J. Appl. Phys.* **54**, 898–905.

Niemann, W., Malzfeldt, W., Rabe, P. and Haensel, R. (1987) Critical cluster size for mixed valence in small matrix-isolated Sm clusters. *Phys. Rev. B* **35**, 1099–1107.

Norman, D., Garg, K. B. and Durham, P. J. (1985) The X-ray absorption near edge structure of transition metal oxides: A one-electron interpretation. *Sol. State Commun.* **56**, 895–8.

Ohta, T., Takeda, H. and Takeuchi, Y. (1982) Mica polytypism: Similarities in the crystal structure of coexisting 1*M* and $2M_1$ oxybiotite. *Am. Mineral.* **67**, 298–310.

Otten, M. T. and Buseck, P. R. (1987) The oxidation state of Ti in hornblende and biotite determined by electron-energy-loss spectroscopy, with inferences regarding the Ti substitution. *Phys. Chem. Minerals* **14**, 45–51.

Pampuch, R. (1971) Le mécanisme de la déshydroxylation des hydroxydes et des silicates phylliteux. *Bull. Grpe franc. Argiles* **23**, 107–18.

Putnis, A. and Güttler, B. (in preparation) TEM studies on the deprotonation and oxidation of biotite.

Robbins, D. W. and Strens, R. G. J. (1968) Polarization dependence and oscillator strength of metal–metal charge-transfer bands in iron (II, III) silicate minerals. *Chem. Comm.* 508–9.

Rossman, G. R. (1984) Spectroscopy of micas. In: *Micas* (Baily, S. W., ed.), *Reviews in Mineralogy* **13**, 145–76.

Rouxhet, P. G., Gillard, J. L. and Fripiat, J. J. (1972) Thermal decomposition of amosite, crocidolite and biotite. *Mineral. Mag.* **38**, 583–92.

Sanz, J., Gonzales-Carreño, T. and Gancedo, R. (1983) On dehydroxylation mechanisms of a biotite in vacuo and in oxygen. *Phys. Chem. Minerals* **9**, 14–8.

Sherman, D. M. (1987) Molecular orbital (SCF-Xα-SW) theory of metal–metal charge transfer processes in minerals. I. Application to Fe^{2+}–Ti^{4+} charge transfer and 'electron delocalization' in mixed valence oxides and silicates. Ibid. **14**, 364–7.

Smith, G., Howes, B. and Hasan, Z. (1980) Mössbauer and optical spectra of biotite: a case of Fe^{2+}–Fe^{3+} interactions. *Phys. Stat. Sol.* (a) **57**, K187–92.

Takeda, H. and Ross, M. (1975) Mica polytypism: Dissimilarities in the crystal structure of coexisting 1*M* and $2M_1$ oxybiotite. *Am. Mineral.* **60**, 1030–40.

Thompson, J. B. (1973) In: Hazen, R. M. and Burnham, C. W. (1973) as cited above.

Tossel, J. A., Vaughan, D. J. and Johnson, K. H. (1974) The electronic structure of rutile, wüstite, and hematite from molecular orbital calculations. *Am. Mineral.* **59**, 319–34.

Vedder, W. and Wilkins, R. W. T. (1969) Dehydroxylation and rehydroxylation, oxidation and reduction of micas. Ibid. **54**, 482–509.

Waychunas, G. A. (1987) Synchrotron radiation XANES spectroscopy of Ti in minerals: Effects of bonding distances, Ti valence, and site geometry on absorption edge structure. Ibid. **72**, 89–101.

——and Rossman, G. R. (1983) Spectroscopic standard

for tetrahedrally coordinated ferric iron: $LiAlO_2$: Fe^{3+}. *Phys. Chem. Minerals* **9**, 212–5.

——Apted, M. J. and Brown, G. E. (1983) X-ray edge absorption spectra of Fe minerals and model compounds: near-edge structure. Ibid. **10**, 1–9.

Wirth, R. (1985) Dehydration of mica (phengite) by electron bombardment in a transmission electron microscope (TEM). *J. Mat. Sci. Lett.* **4**, 327–30.

[*Manuscript received 18 January 1989; revised 20 April 1989*]